

# Dynamics of Translational Friction in Needle–Tissue Interaction During Needle Insertion

ALI ASADIAN,<sup>1,2</sup> RAJNI V. PATEL,<sup>1,2,3</sup> and MEHRDAD R. KERMANI<sup>1,2</sup>

<sup>1</sup>Canadian Surgical Technologies and Advanced Robotics (CSTAR), Lawson Health Research Institute, London, ON, Canada; <sup>2</sup>Department of Electrical and Computer Engineering, Western University (UWO), London, ON, Canada; and <sup>3</sup>Department of Surgery, Western University (UWO), London, ON, Canada

(Received 10 May 2013; accepted 10 August 2013; published online 21 August 2013)

Associate Editor Bahman Anvari oversaw the review of this article.

**Abstract**—In this study, a distributed approach to account for dynamic friction during needle insertion in soft tissue is presented. As is well known, friction is a complex nonlinear phenomenon. It appears that classical or static models are unable to capture some of the observations made in systems subjected to significant frictional effects. In needle insertion, translational friction would be a matter of importance when the needle is very flexible, or a stop-and-rotate motion profile at low insertion velocities is implemented, and thus, the system is repeatedly transitioned from a pre-sliding to a sliding mode and vice versa. In order to characterize friction components, a distributed version of the LuGre model in the state-space representation is adopted. This method also facilitates estimating cutting force in an intra-operative manner. To evaluate the performance of the proposed family of friction models, experiments were conducted on homogeneous artificial phantoms and animal tissue. The results illustrate that our approach enables us to represent the main features of friction which is a major force component in needle–tissue interaction during needle-based interventions.

**Keywords**—Needle–tissue friction, Robot-assisted needle insertion, Needle-based interventions.

## INTRODUCTION AND PRIOR WORK

Flexible needles that can facilitate curved trajectories are of importance in a number of percutaneous applications: brachytherapy, anesthesia, tissue/fluid sampling, ablation, neurosurgery, and deep brain stimulation particularly in regions that are difficult to access. However, precise placement of a needle tip is a difficult task, and deviation of the needle tip from its

intended target area can degrade the effectiveness of the therapy, lead to misdiagnosis or tissue damage. Thus, accurate and dexterous targeting is important in percutaneous procedures, and robotics-assisted needle steering for tip positioning at specific targets inside soft tissue has become an active research area.<sup>1</sup>

In order to design a needle steering strategy, the needle is likely to be stopped or slowed down and then rotated before inserting further.<sup>2,13</sup> Thus, the interaction between the needle and living tissue which is velocity-dependant and includes frictional features has to be thoroughly studied. In this paper, we formulate a model of translational friction so as to investigate the dynamic behavior of distributed friction along the contact patch when the needle interacts with an elastic medium. In the future, adding full frictional components as developed in this paper to real-time beam-based bending models,<sup>2,4</sup> and incorporating the refined deflection mechanism into path planners<sup>2,3,13,28</sup> are expected to yield better needle steering. This will allow the guidance of highly steerable needles or needle-like structures with enhanced steerability. This is the main motivation in this study.

Several studies have been performed dealing with the measurement and the modeling of force components involved in needle–tissue interaction while a comprehensive analytical model for distributed friction in percutaneous interventions is lacked. Misra *et al.*<sup>19</sup> provided an extensive review on tool-tissue interaction, and Van Gerwen *et al.*<sup>26</sup> presented a comprehensive survey of the empirical aspects of needle–tissue interaction forces. As a pioneering study for force modeling in needle insertion, Okamura *et al.*<sup>20</sup> proposed an empirical force model based on which the total insertion force was composed of capsule stiffness force, friction and cutting forces. In this study, friction was

Address correspondence to Ali Asadian, Department of Electrical and Computer Engineering, Western University (UWO), London, ON, Canada. Electronic mails: aasadian@uwo.ca, rvpatel@uwo.ca, and mkermani@eng.uwo.ca

described by a modified Karnopp model which was comprised of a viscous term plus a constant static friction within a dead zone in the vicinity of zero. Asadian *et al.*<sup>5</sup> introduced a compact nonlinear dynamic model plus a feasible identification procedure to model the total axial insertion force in terms of the insertion depth. Kataoka *et al.*<sup>15</sup> measured the involved forces and analyzed them qualitatively without any explicit quantification, and Podder *et al.*<sup>22</sup> derived a statistical model to estimate the maximum insertion force during prostate brachytherapy. In, Barbe *et al.* employed the Kelvin–Voigt (KV) model in order to reconstruct force evolution during needle insertion, and possibly due to ignoring frictional terms, an accurate bio-mechanical model could not be found in an on-line manner. Hing *et al.*<sup>14</sup> predicted the insertion force by relating needle–tissue interaction force to tissue deformation, and using a linear elastic finite element method (FEM). This analysis led to extraction of important parameters for modeling tissue puncture and relaxation, but not for friction. The translational friction along the insertion depth was ignored in order to present a static model for needle deflection in Abolhassani *et al.*<sup>2</sup> The results were relatively convincing. However, the assumption is not valid when the needle is very flexible, or frictional effects are significant. Ignoring the impact of friction, Webster *et al.*<sup>27</sup> also developed an experimental bending model for insertion a flexible bevel-tip needle in stiff rubber. This concept of fitting a constant curvature to the needle path was then employed to guide the needle.<sup>3,13</sup>

In general, research on systems with friction has a long and rich history.<sup>21</sup> At this point, the authors believe that the complexity of the friction mechanism in needle insertion deserves further detailed examination to develop a feasible solution. In,<sup>4,24</sup> and in the context of bending modeling, only the viscous translational friction was studied. With regard to rotational friction, Reed *et al.*<sup>23</sup> developed a mechanics-based approach using the KV interaction model, FEM, and the Karnopp friction model to predict the tip lag for a rotating needle inside tissue. In the current work as an extension of our preliminary work,<sup>6</sup> we will study the translational frictional force in needle insertion. The essence of our approach is inspired by the physically-based method presented by Canudas *et al.*<sup>11</sup> for modeling longitudinal road-tire interaction in ground vehicles. In this study, we develop a solution that is feasible to implement, and is well suited for interventional procedures.

The remainder of this paper is organized as follows. In section “[Proposed Lugre-Based Structures](#),” the proposed methodology is described while section “[Experimental Studies](#)” introduces our test-bed followed by experimental evaluation. Finally, section

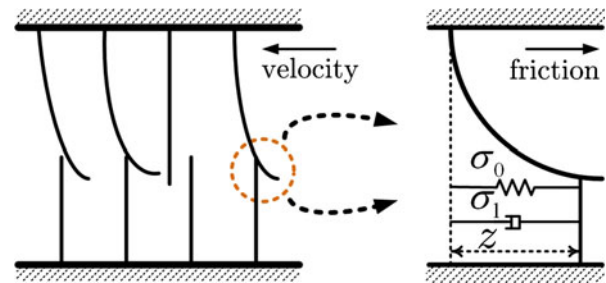


**FIGURE 1.** Microscopic representation of irregular contact surfaces and elastic bristles whose bending gives rise to the distributed friction.

“[Concluding Remarks and Future Work](#)” presents conclusions and suggestions for future work.

## PROPOSED LUGRE-BASED STRUCTURES

Several studies have explored different aspects of friction.<sup>10,11,21</sup> Friction does not have an instantaneous response, but has internal dynamics. That is why dynamic models such as the LuGre model have been widely employed in the literature.<sup>10,11,16,21</sup> In our application, the conventional point LuGre model<sup>10,21</sup> can be extended to a distributed version along the inserted portion of the needle (the area of contact or patch). In brief, Model I is a static LuGre-based structure and Model II is a lumped version while Model III introduces a distributed dynamic nature in the following.

To this end, let  $z(\zeta, t)$  denote the model’s internal state or the deflection of the bristle elements located at the longitudinal position  $\zeta$  at a certain time  $t$ . Fig. 1 also helps us to get more insight into the principle of this model which is based on the deflection of spring-like bristles at the microscopic level of moving surfaces. The governing equation is, therefore, written as follows<sup>11</sup>:

$$\begin{cases} \frac{dz}{dt}(\zeta, t) = v - \frac{\sigma_0|v|}{g(v)}z \\ F_{\text{friction}}(t) = \int_0^{L(t)} dF(\zeta, t) \end{cases} \quad (1)$$

$$g(v) = \mu_c + (\mu_s - \mu_c)e^{-\alpha|v|^{\beta}} \quad (2)$$

$$dF(\zeta, t) = \left\{ \sigma_0 z(\zeta, t) + \sigma_1 \frac{\partial z}{\partial t}(\zeta, t) + \sigma_2 v \right\} dF_n(\zeta, t) \quad (3)$$

where  $dF(\zeta, t)$  is the differential friction force developed in the element  $d\zeta$ , and  $dF_n(\zeta, t)$  is the differential normal force applied to the same element at time  $t$ . Herein,  $v$  is the contact velocity of each differential element, and  $L$  is the current insertion distance.

As observed, the total contact friction in Eq. (1) is characterized by five static coefficients namely

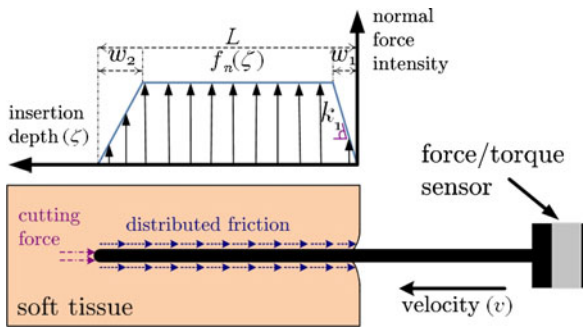


**FIGURE 2.** Macroscopic representation of needle–tissue interaction and involved force components with a fully trapezoidal force intensity distribution.

$\mu_c$ ,  $\mu_s$ ,  $\sigma_2$ ,  $\alpha$ , and  $\gamma$ , and two dynamic parameters:  $\sigma_0$  and  $\sigma_1$ .  $\sigma_0$  can be understood as being the stiffness coefficient of the microscopic deformations during the pre-sliding displacement, and  $\sigma_1$  as being the damping coefficient associated with  $\dot{z}$ .  $\sigma_2$  is the viscous relative damping while  $\mu_c$  and  $\mu_s$  are the normalized Coulomb and stiction friction, respectively. The function  $g$  also generates the classical Stribeck effect in which the parameter  $\gamma$  is used to achieve desirable steady-state behavior. For more details, see Canudas De Wit *et al.*<sup>10</sup> In the following and prior to experimental validation, we derive three versions of the sought translational friction model during needle insertion.

Assuming a steady-state normal force distribution and introducing a normal force intensity function  $F_n(\zeta)$  (force per unit length) along the patch as shown in Fig. 2, we have  $dF_n(\zeta, t) = dF_n(\zeta) = F_n(\zeta)d\zeta$ . Note that the friction force acts on the side wall of the needle shaft in the axial direction while the clamping force is applied in the normal direction. The latter force is the impact of tissue resistance, and is influenced by the incision shape created by the needle tip and its size as well as the tissue elasticity. The cutting force is separately treated as a concentrated load at the tip<sup>20</sup> that is beyond the scope of our discussion. Thus, the tangential friction force is given by

$$F_{\text{friction}}(t) = \int_0^{L(t)} \left\{ \sigma_0 z(\zeta, t) + \sigma_1 \frac{\partial z}{\partial t}(\zeta, t) + \sigma_2 v \right\} F_n(\zeta) d\zeta \quad (4)$$

Setting  $\frac{dz}{dt}(\zeta, t) = \frac{\partial z}{\partial \zeta} \frac{\partial \zeta}{\partial t} + \frac{\partial z}{\partial t} = \frac{\partial z}{\partial \zeta} v + \frac{\partial z}{\partial t}$  in (1) renders the following equation that has to be solved both in time and space to find a closed-form relationship to account for the friction.

$$\frac{\partial z}{\partial \zeta}(\zeta, t) = 1 - \text{sign}(v) \frac{\sigma_0}{g(v)} z - \frac{1}{v} \frac{\partial z}{\partial t}(\zeta, t) \quad (5)$$

Assuming the deflection of the first bristle element to be zero imposes the boundary condition as  $z(0, t) = 0$  for  $\forall t \geq 0$ . In a quasi-static condition where  $\frac{\partial z}{\partial t}(\zeta, t) \simeq 0$  within a small enough interval of time, (5) is reduced to

$$\frac{\partial z}{\partial \zeta}(\zeta, t) = 1 - \text{sign}(v) \frac{\sigma_0}{g(v)} z \quad \zeta \in (0, L) \quad (6)$$

The solution of the ordinary differential equation (ODE) defined in (6) is expressed as below, and can suitably approximate the solution of the equation introduced in (5). It is assumed in (6) that the bristles have a faster dynamic response compared to variations of the insertion velocity.

$$z_{qs} = \frac{g(v)}{\sigma_0} \left( 1 - e^{-\frac{\sigma_0 \zeta}{g(v)}} \right) \text{sign}(v) \quad (7)$$

$$F_{qs} = \int_0^L \{ \sigma_0 z_{qs} + \sigma_2 v \} F_n(\zeta) d\zeta \quad (8)$$

To calculate the steady-state solution defined by (8), it is required to know the distribution of the force density function  $f_n(\zeta)$ . For the sake of simplicity, the first step is to presume a uniform load intensity where  $f_n(\zeta) = F_n/L$  for  $\zeta \in (0, L)$ . Here,  $F_n$  stands for the total normal load along the shaft. This particular choice agrees with the constant estimated force density along the needle shaft reported in DiMaio and Salcudean.<sup>12</sup> Due to the symmetry resulting from the use of a cone-tip needle, the force peak at the tip that can be attributed to the tissue cutting force<sup>12</sup> is ignored here. Therefore, the quasi-static solution, namely Model I, is expressed as

$$F_{qs} = \left( \text{sign}(v) g(v) \left[ 1 - \frac{g(v)}{\sigma_0 L} \left( 1 - e^{-\frac{\sigma_0 L}{g(v)}} \right) \right] + \sigma_2 v \right) F_n \quad (9)$$

Following this strategy and by fitting the above steady-state representation to experimental data, the unknown parameters except  $\sigma_1$  can be identified. As another numerical approximation that is proposed at this point, the distributed model introduced by (1) agrees with a lumped model assuming that the patch region is not changing with respect to time, or the bristles are moving much faster than the needle itself. A mean friction state is defined as follows<sup>11</sup>:

$$\tilde{z}(t) = \frac{\int_0^L z(\zeta, t) f_n(\zeta) d\zeta}{F_n} \quad (10)$$

where  $F_n = \int_0^L f_n(\zeta) d\zeta$ . Following a few algebraic manipulations and applying the chain rule using (5) and (10) the friction model in terms of  $\tilde{z}$  is given by (11). In the following, the first and last terms on the

right-hand side of (12) represent the effect of the boundary conditions while the term under the integral describes the impact of the lateral force distribution.

$$\begin{cases} \dot{\tilde{z}} = v - \left( \text{sign}(v) \frac{\sigma_0}{g(v)} - \beta(t) \right) v \tilde{z} \\ F_{\text{friction}}(t) = F_n(\sigma_0 \tilde{z} + \sigma_1 \dot{\tilde{z}} + \sigma_2 v) \end{cases} \quad (11)$$

$$\beta(t) = \frac{1}{F_n \tilde{z}} \left( z(0, t) f_n(0) + \int_0^L z(\zeta, t) \frac{\partial f_n(\zeta)}{\partial \zeta} d\zeta \right) - \frac{f_n(L)}{F_n} \quad (12)$$

This approximation is called the averaged lumped model. Setting  $\frac{\partial f_n}{\partial \zeta}(\zeta) = 0$  in (12) due to the assumption of a uniform load distribution with zero-force boundary conditions, i.e.,  $f_n(0) = f_n(L) = 0$ , yields  $\beta(t) = 0$ . This assumption is borrowed from the fact that a realistic solution, by continuity, provides zero normal force at the boundaries of the contact area. A trapezoidal force profile that fully satisfies these conditions may be a more realistic choice. However, the main reason for setting  $f_n(\zeta)$  to be uniform along the shaft with zero force intensity at the boundaries is to reduce the identification complexity. Thus, we obtain Model II as

$$\begin{cases} \dot{\tilde{z}} = v - \frac{\sigma_0 |v|}{g(v)} \tilde{z} \\ F_{\text{friction}}(t) = F_n(\sigma_0 \tilde{z} + \sigma_1 \dot{\tilde{z}} + \sigma_2 v) \end{cases} \quad (13)$$

This feasible and dynamic scheme denoted by (13) is in fact the conventional point-contact LuGre model, and will be used in the sequel as employed in Kermani *et al.*<sup>16</sup> However, in order to more precisely incorporate the effect of distributed needle-tissue interaction, and introduce the third friction model,  $\beta$  should not be ignored from the friction calculations. The function  $\beta$  captures the distributed nature of translational friction, and is determined according to the postulated functional form of  $f_n(\zeta)$ . Toward this goal, let us assume that  $z(\zeta, t)$  can be decomposed into two time-independent and space-independent components  $\psi(\zeta)$  and  $\phi(t)$ , respectively.<sup>11</sup> Hence,  $z(\zeta, t) = \psi(\zeta)\phi(t)$  for  $0 \leq \zeta \leq L(t)$  and  $t \geq 0$ , and  $\beta(t)$  is rewritten by replacing  $L$  with  $L(t)$  in (12), and applying the zero-force boundary conditions.

$$\beta(t) = \frac{\int_0^{L(t)} \psi(\zeta) f_n(\zeta) d\zeta}{\int_0^{L(t)} \psi(\zeta) f_n(\zeta) d\zeta} \quad (14)$$

For a trapezoidal distribution that is a realistic assumption, the normal force intensity function can be defined by a set of five parameters, namely  $k_1, k_2, w_1, w_2$  and  $f$  as in (15). In case of a symmetrical distribution, we have  $w_1 = w_2 = w, k_1 = f/w$ , and

$k_2 = Lf/w$  ( $w \neq 0$ ) in Fig. 2. Note that it is rational to assume that the bristles are gradually deflected along the contact patch. In addition, for the first differential bristle-like element at the skin entry point, the amount of deflection is zero as assumed previously.

$$f_n(\zeta) = \begin{cases} k_1 \zeta & 0 \leq \zeta \leq w_1 \\ f & w_1 \leq \zeta \leq L(t) - w_2 \\ -k_1 \zeta + k_2 & L(t) - w_2 \leq \zeta \leq L(t) \end{cases} \quad (15)$$

Thus,  $\psi(\zeta) = \zeta^\lambda$  ( $0 \leq \zeta \leq L(t), \lambda > 0$ ) is a good candidate to represent the deflection function  $\psi$  in (14). Next, introducing (15) into (14) yields the sought function  $\beta(t)$ . Thus,  $\beta(t)$  is approximated using either (16) or (17).

$$\beta_1(t) \approx \begin{cases} \frac{\frac{\lambda+2}{\lambda+1} \frac{1}{L(t)}}{(\lambda+2)w^{\lambda+1}} & 0 < L(t) \leq w \\ \frac{(\lambda+2)w^{\lambda+1}}{(\lambda+2)L(t)^{\lambda+1}-w^{\lambda+1}} & L(t) > w \end{cases} \quad (16)$$

$$\beta_2(t) \approx \begin{cases} \frac{-2(\lambda+2)(2^\lambda-1)}{2^{\lambda+1}-1} \frac{1}{L(t)} & 0 < L(t) \leq 2w \\ -\frac{(L(t)-w)^{\lambda+1}+w^{\lambda+1}-L(t)^{\lambda+1}}{(L(t)-w)^{\lambda+2}+w^{\lambda+2}-L(t)^{\lambda+2}} (\lambda+2) & L(t) > 2w \end{cases} \quad (17)$$

In (16),  $w = w_1$ , and  $w_2$  was set to zero while in (17), the function  $f_n$  was assumed to have symmetrical form in which  $w = w_1 = w_2$ . In both cases, at  $t = t_k$ , the force intensity profile converts to the trapezoidal functional form from the triangular functional shape as it is for  $t < t_k$ . In our setting, the functions  $\beta_1(t)$  and  $\beta_2(t)$  correspond to right and isosceles trapezoids, respectively. Accordingly, Figs. 3a and 3b show the transition of the force profiles as the needle is inserted into the tissue. In both figures, the dashed circles represent insertion states. States 1 to 3 associate with the growing triangular forms while state 4 is a boundary state, and state 5 denotes the full trapezoidal shape as  $t > t_k$ . The validity of presuming such force intensity profiles will be investigated later on through experimental work.

Obtaining an explicit expression for the function  $\beta(t)$  enables us to complete the distributed dynamic LuGre model represented in (11), and thereby forming Model III. Model III is an extension of Model II in which  $\beta(t)$  is not zero. It is not difficult to show that (14) and therefore (16) or (17) hold valid for a time-varying insertion velocity. It occurs when the zero-force boundary conditions are satisfied for each differential element at each time instant. Thus, all mathematical terms containing  $\dot{L}(t)$  are set to zero toward deriving the closed-form representation of  $\beta(t)$ . This assumption is valid when the bristles have fast dynamics relative to the insertion speed.

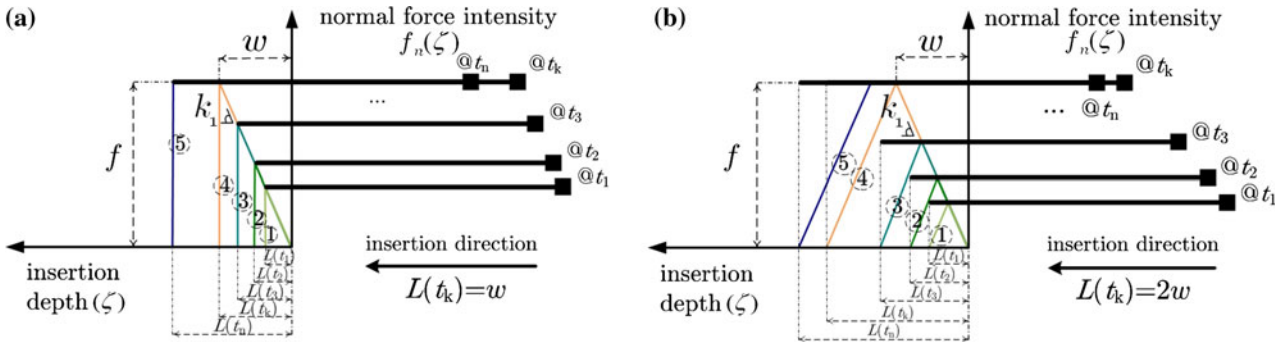


**FIGURE 3.** Evolution of the triangular/trapezoidal interaction force distribution associated with: (a)  $\beta_1$  in Model III-A, (b)  $\beta_2$  in Model III-B.

At this point, the measurement equation expressing the distributed friction is revisited in order to fit it into the new state-space model. Equation 4 can be rewritten as

$$F_{\text{friction}}(t) = \int_0^{L(t)} \left\{ (\sigma_0 - \frac{\sigma_0 \sigma_1 |v|}{g(v)}) z(\zeta, t) - \sigma_1 v \frac{\partial z}{\partial \zeta}(\zeta, t) + (\sigma_1 + \sigma_2) v \right\} F_n(\zeta) d\zeta \quad (18)$$

Knowing that  $\int_0^{L(t)} z(\zeta, t) f_n(\zeta) d\zeta = \tilde{z}(t) \times \int_0^{L(t)} f_n(\zeta) d\zeta = \tilde{z}(t) \times F_n$ , and applying the zero-force boundary conditions, we obtain the following set of equations for Model III in which  $\tilde{x}(t)$  stands for the patch length  $L(t)$  that can be time-varying. In the current state-space representation (19), labeled henceforth as Model III-B, the  $\beta$  function was approximated using  $\beta_2$  as in (17). A similar structure can be simply obtained by the use of  $\beta_1$  (Model III-A).

$$\begin{cases} \dot{\tilde{x}} = v \\ \dot{\tilde{z}} = \begin{cases} v - \frac{\sigma_0}{g(v)} |v| \tilde{z} - \frac{2(\lambda+2)(2^\lambda-1)}{2^{\lambda+1}-1} \tilde{x} & 0 < \tilde{x} \leq 2w \\ v - \frac{\sigma_0}{g(v)} |v| \tilde{z} - \frac{(\tilde{x}-w)^{\lambda+1} + w^{\lambda+1} - \tilde{x}^{\lambda+1}}{(\tilde{x}-w)^{\lambda+2} + w^{\lambda+2} - \tilde{x}^{\lambda+2}} (\lambda+2)v\tilde{z} & \tilde{x} > 2w \end{cases} \\ F_{\text{friction}}(t) = f(\tilde{x} - w) \left\{ \left(1 - \frac{\sigma_1 |v|}{g(v)}\right) \sigma_0 \tilde{z} - \sigma_1 \dot{\tilde{z}} + (\sigma_1 + \sigma_2) v \right\} \end{cases} \quad (19)$$

## EXPERIMENTAL STUDIES

### Setup Description

An experimental implementation of the proposed methodology was carried out on a 5-degree-of-freedom (DOF) double parallelogram robotic system fully designed and manufactured in our group<sup>9</sup> (Fig. 4). A Nano43 6-DOF force/torque sensor (ATI Industrial Automation) was attached to the needle holder to measure the force signals acting on the needle shaft whose high frequency contents were eliminated by a moving average filter at the rate of 200 Hz. Using a

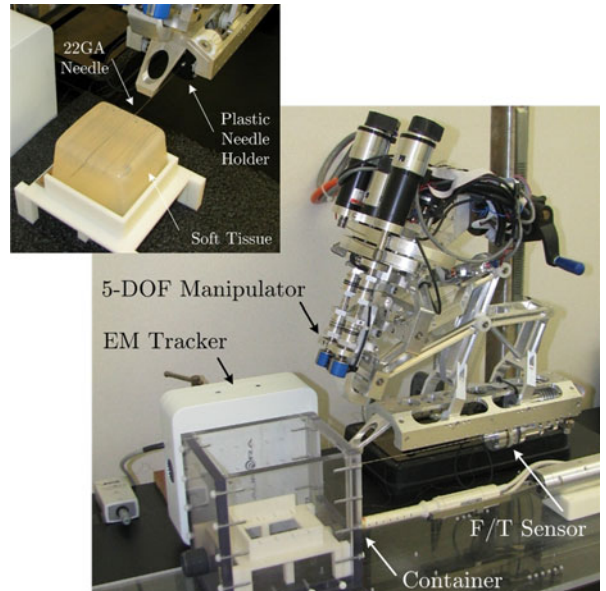


**FIGURE 4.** A view of our needle insertion robotic system.

compression test,<sup>25</sup> Young's modulus  $E$  of an examined phantom was also estimated from the force-deformation mapping of the sample with known geometry. In our test-bed, needle A represents the cannula of an 18 GA needle (Cook Medical) while needle B denotes the cannula of a 22 GA needle (Covidien). Needle B is more flexible than needle A both of which are with conical tip.

### Friction Identification Using an Artificial Phantom

We start validating the proposed friction structure with a detailed description of our artificial phantom study. A similar procedure was applied to organic tissue that will be explained in section “[Friction Identification in Organic Tissues](#).<sup>26</sup>” The artificial phantom was made from Gelrite Gellan Gum (Sigma-Aldrich) with two different concentrations in water: 4% (tissue A,  $E = 0.11$  MPa, less stiff) and 6% (tissue

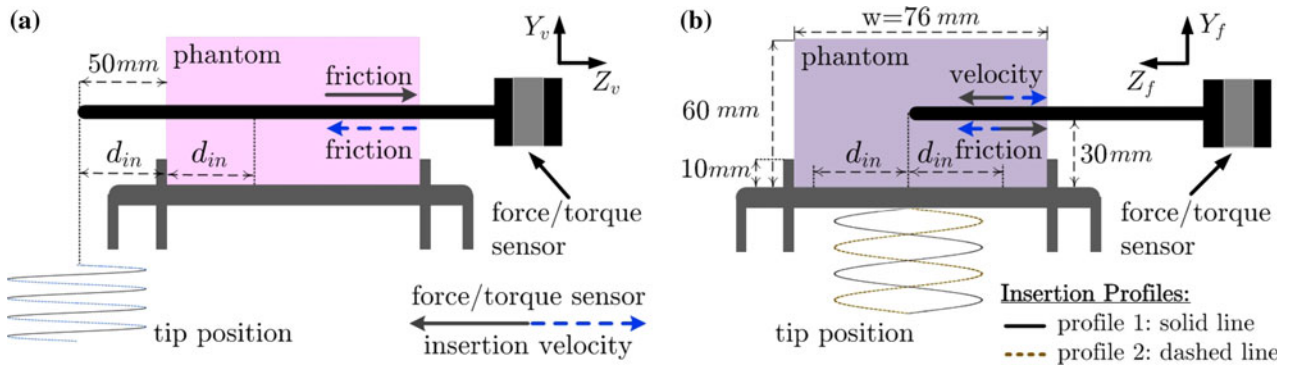


**FIGURE 5.** Needle insertion profiles: (a) periodic insertion profile for friction identification, (b) cyclic insertion profiles for friction estimation.

B,  $E = 0.16$  MPa, more stiff). This powder simulated a uniform elastic environment, and created a watery medium that made the experiments more realistic in terms of the measured force ranges and viscosity.

In order to identify the models' parameters, the system was excited in the axial direction by applying a low-frequency sinusoidal torque. The frequency and the amplitude of the insertion signal was selected so that it could transition the system from the pre-sliding to the sliding phase and vice versa. The proper selection required a few trials and errors. We examined a translational motion profile whose maximum amplitude ( $d_{in}$ ) lied between 10 and 50 mm and its frequency ( $f_{in}$ ) ranged from 0.02 to 0.2 Hz. In our setting,  $\gamma$  was assumed to be 1 in (2) as the most commonly used value,<sup>11</sup> and without loss of generality,  $F_n$  was set to 1 N.

For identification, the needle was inserted from one side into the phantom so that the tip was placed 5 cm outside of the tissue. Each artificial phantom with a known thickness ( $w = 76$  mm) was placed into a container and clamped such that the bottom of the tissue was rigidly fixed (see Fig. 5). The insertion height was approximately adjusted to 30 mm, while the phantoms were fabricated at the total height of 60 mm. In the identification test shown in Fig. 5a, the tip is not cutting the tissue and there exists a constant amount of tissue in contact with the needle shaft. Fig. 5b in addition corresponds to the prediction test in which the needle tip is initially placed in a middle point inside the phantom. It will be later on revisited in section “Friction Prediction and Cutting Force Estimation.”

The total axial force ( $F_z$ ) measured by the F/T sensor is expressed as the sum of inertial and interaction forces. The interaction force is composed of a cutting force at the tip and distributed friction along the needle. The estimated acceleration profile ( $a$ ) and mass of each needle plus its holder ( $m$ ) are known. The mass values for the 18 and 22 GA needles were measured to be 44.058 and 13.128 g, respectively.

Thus, according to the reference frames of the force sensor and the robot's end-effector expressed in Fig. 5, we have  $F_{\text{interaction}} = F_z(\text{measured}) + ma$ .

Note that clinical insertion rates are usually kept low (less than  $10 \text{ mm s}^{-1}$ ) mainly due to safety considerations.<sup>12</sup> One practical issue of applying low velocities and accelerations is that ordinary differentiation to compute joint velocities from encoder readings leads to high computational noise. Thus, to reduce this noise which can become dominant, a high-gain observer has been implemented to estimate the velocity from the encoder measurements. The details of observation and velocity estimation have been discussed in<sup>7</sup> where we took advantage of dynamic observation to compensate for soft tissue motion during friction identification. Needle–tissue relative velocity compensation is essential particularly in highly deformable tissue (section “Friction Identification in Organic Tissues”) since frictional effects in general depend on the relative velocity between moving contacts.

Having obtained a friction–velocity cycle, the parameters of the models proposed in the previous section can be identified. Due to the additional term  $\beta(t)$  in our equations, many of existing adaptive or advanced friction identification techniques<sup>16</sup> are not applicable here. Hence, we employed MATLAB built-in functions and system identification toolbox to find the unknown parameters of each introduced model. In brief, each structure, i.e., Models I, II, and III, was defined as a nonlinear state-space gray-box model. The specified object then underwent parameter estimation using an iterative prediction-error minimizer, and an adaptive Gauss–Newton search method.

Initially, a sensitivity test was performed. Four values were selected for  $\lambda$ , and Model III was identified in each case for  $w = 2.5$  mm. Fig. 6a compares the outcome of each parameter selection for Model III-B. According to our research, it is likely that by optimizing Model III in terms of  $\lambda$  over the entire

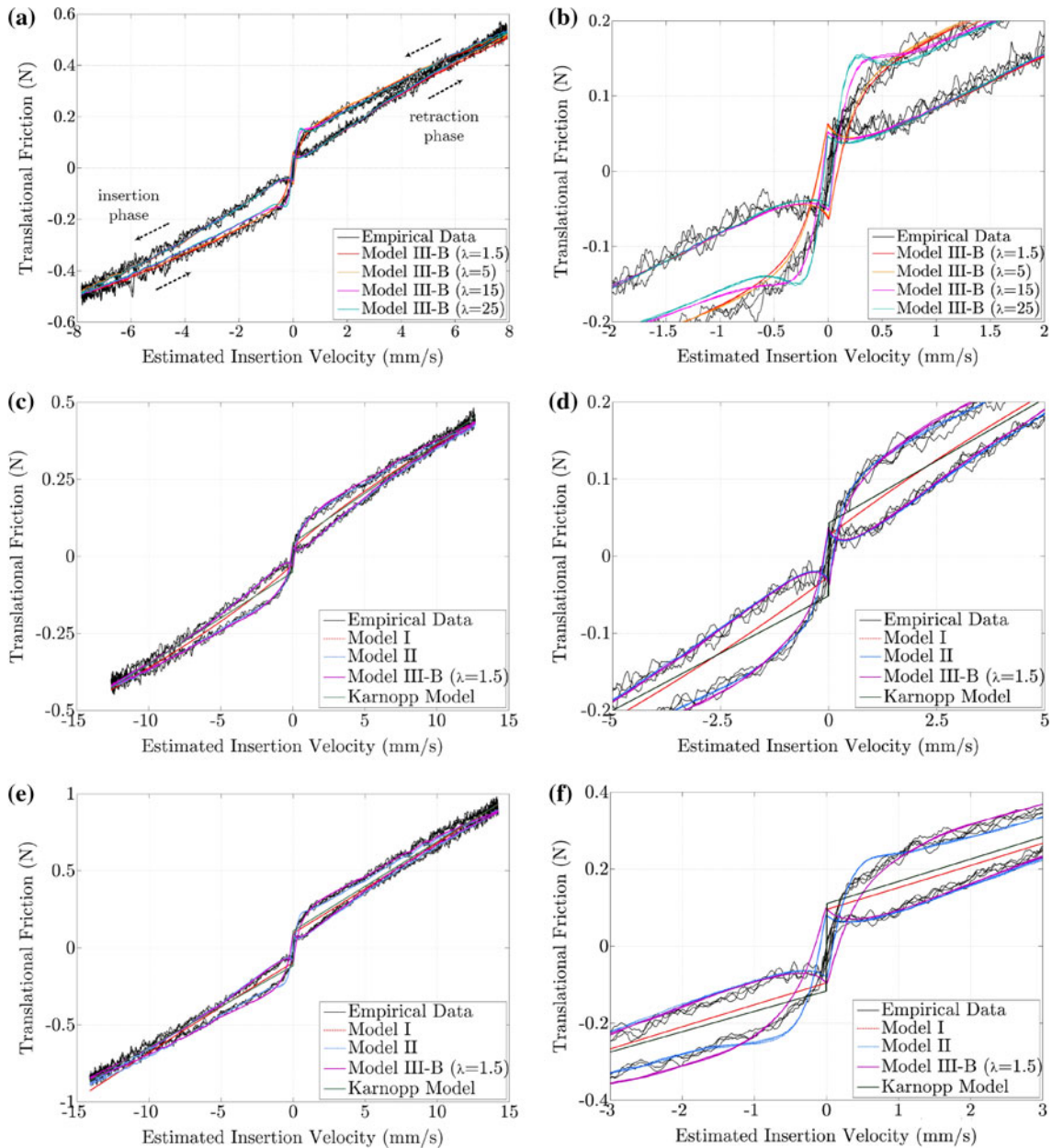


**FIGURE 6. Identified and experimental friction–velocity cycle: Model III-B with variable  $\lambda$ , needle A/tissue A,  $f_{in} = 0.05$  Hz, and  $d_{in} = 25$  mm: (a)  $-8 \text{ mm s}^{-1} \leq v \leq 8 \text{ mm s}^{-1}$ , (b)  $-2 \text{ mm s}^{-1} \leq v \leq 2 \text{ mm s}^{-1}$ . Identified and experimental friction–velocity cycle in case 2: (c)  $-15 \text{ mm s}^{-1} \leq v \leq 15 \text{ mm s}^{-1}$ , (d)  $-5 \text{ mm s}^{-1} \leq v \leq 5 \text{ mm s}^{-1}$ . Identified and experimental friction–velocity cycle in case 4: (e)  $-15 \text{ mm s}^{-1} \leq v \leq 15 \text{ mm s}^{-1}$ , (f)  $-3 \text{ mm s}^{-1} \leq v \leq 3 \text{ mm s}^{-1}$ .**

range of [0.5, 5], friction estimation can be improved further. For the sake of brevity, this task is omitted from this paper and will be reported in a future publication. Henceforth, it is assumed that this tuning parameter is selected from the set {0.5, 2.5, 1.5, 5} such that the estimation error is minimized. In Fig. 6a, the best performance was achieved by setting  $\lambda$  to 5. In addition, Model III-A mimicked a very identical performance but with a different selection for  $\lambda$ ; thus, it has been ignored from presentation in this section. In

section “Friction Prediction and Cutting Force Estimation” when the inserted length of the needle changes with the passage of time, Model III-A will be assessed further.

Table 1 defines the test conditions of four studied cases, and Figs. 6b and 6c present two estimated friction–velocity mappings using the introduced LuGre-based techniques. For comparison, the modified Karnopp model was also implemented.<sup>20</sup> Briefly, this static benchmark includes only viscous and Coulomb

TABLE 1. Test conditions of four case studies.

	Case 1	Case 2	Case 3	Case 4
$f_{in}$ (Hz)	0.05	0.08	0.02	0.05
$d_{in}$ (mm)	25	25	45	45
Needle/tissue combination	Needle A + tissue A	Needle B + tissue A	Needle A + tissue B	Needle B + tissue B

terms whose corresponding coefficients were estimated by a simple least-squares method. We studied the logged data over four periodic cycles, and repeated each test as described at four different insertion points. The plots show that Models II and III are capable of capturing the dynamic behavior of friction including the Stribeck effect and the hysteresis loop as opposed to the Karnopp model and Model I. Note that the inset subplots in the graphs are the magnified versions of the original plots in the region of the origin in order to better visualize the data. Tables 2, 3, and 4 summarize the estimated parameters. The reported results are the averaged values expressed as mean  $\pm$  standard deviation ( $\sigma$ ). By comparison, the parameter  $\sigma_0$  had the most inconsistency. Estimation of  $\mu_s$  could exhibit a similar behavior depending on the insertion profile and the employed needle–tissue combination.

Table 5 lists the root mean squared error (RMSE) values of friction estimation in the four considered cases. To further assess the performance of each model, RMSE values were separately evaluated in two ranges of insertion velocities labeled low and high range. The low range was associated with the velocities whose absolute values lied in the interval  $[0, 0.5v_{max}]$  while the high range covered the interval  $[0.5v_{max}, v_{max}]$ . Here,  $v_{max}$  denotes the maximum insertion velocity of each motion profile. It is emphasized again that in each experiment, Model III should be optimized in advance in terms of the parameter  $\lambda$ . We defined the same RMSE value as our objective function, and examined the four quantities in each case study to select the best  $\lambda$  value.

In general, the dynamic structures, e.g., Models II and III, outperformed the static models. By comparison, the Karnopp model showed better overall performance than Model I which was the static version of the LuGre model. Nevertheless, Model I provided a slightly better prediction for the low range velocities in cases 1, 2, and 4. Model I also exhibited an exponential growth of error in terms of velocity that was more apparent in Fig. 6c (for  $v \leq -10 \text{ mm s}^{-1}$ ). At higher velocities, Model III-B performed better in contrast to Model II, and surprisingly, the Karnopp model outperformed Model II in cases 3 and 4 (the second half of Table 5). Considering all the models and cases studied, Model III-B excelled overall as shown. This suggests

that the isosceles trapezoidal force density function in needle insertion serves better than the right trapezoidal density assumption. To remind, see Fig. 3. However, in the vicinity of zero velocity, Model II depicted the friction loop the best in case studies 1 and 4 according to the low-range error values reported in Table 5. This better accuracy originates from the faster transient response provided by Model II that is visible in the upper-left graph in Fig. 6c.

In our observations, unexpected fluctuations in the empirical data should not come as a surprise. In practice, it was not easy to fabricate a completely homogeneous phantom using Gellan gum, and air bubbles spread over the volume of the phantom prevented the medium from being fully uniform.

#### Friction Prediction and Cutting Force Estimation

Having identified the models, the estimated parametric values (specified in Tables 2, 3, and 4) were fed into the selected lumped or distributed model in order to predict the friction force along the time-varying insertion length. In this experiment, the needle tip was initially placed inside the phantom so that  $L_0 = 0.5w = 38 \text{ mm}$  (see Fig. 5b). In the first motion profile illustrated by a solid line, the needle was inserted until it approached the left wall of the container and then it was retracted toward the right wall. In the second profile denoted by a dashed line in the same plot, the tip motion had an opposite periodic sequence. To conduct the experiments, needle B was inserted into tissue A and tissue B respectively at the rates of 0.05 and 0.08 Hz ( $d_{in} = 25 \text{ mm}$ ). Here, they are referred to as cases 1 and 2. Testing other combinations was possible, but without loss of generality, we limited our observations to only two case studies. Fig. 7 compares the measured interaction force with the predicted friction forces in the second case study, and Table 6 reports the numerical results in which major cutting was excluded from RMSE calculations.

Generally speaking, the cutting mechanism, as the most obvious non-frictional behavior during needle insertion, has not been well formulated heretofore. The cutting force at the needle tip (Fig. 2) is influenced by complex factors, e.g., tip shape and tissue properties, in practice. As mentioned before, the measured axial force denotes the summation of friction, cutting force,

**TABLE 2. Estimated parameters of Model I.**

	Case 1	Case 2	Case 3	Case 4
$\sigma_0$ (N mm $^{-1}$ )	1.272 ± 0.338	0.616 ± 0.098	1.903 ± 0.125	0.812 ± 0.044
$\sigma_2$ (N s)	0.017 ± 0.005	0.015 ± 0.002	0.011 ± 0.002	0.030 ± 0.003
$\mu_s$ (N)	0.711 ± 0.116	0.338 ± 0.148	0.715 ± 0.090	0.653 ± 0.055
$\mu_c$ (N)	0.044 ± 0.011	0.024 ± 0.003	0.055 ± 0.003	0.058 ± 0.009
$\alpha$ (s mm $^{-1}$ )	0.081 ± 0.007	0.077 ± 0.024	0.121 ± 0.018	0.073 ± 0.010

**TABLE 3. Estimated parameters of Model II.**

	Case 1	Case 2	Case 3	Case 4
$\sigma_0$ (N mm $^{-1}$ )	1.344 ± 0.214	0.592 ± 0.224	1.877 ± 0.104	0.813 ± 0.132
$\sigma_1$ (N s mm $^{-1}$ )	0.463 ± 0.013	0.239 ± 0.055	0.686 ± 0.045	0.312 ± 0.037
$\sigma_2$ (N s)	0.016 ± 0.003	0.012 ± 0.002	0.011 ± 0.000	0.031 ± 0.002
$\mu_s$ (N)	0.735 ± 0.087	0.448 ± 0.082	0.669 ± 0.073	0.633 ± 0.029
$\mu_c$ (N)	0.034 ± 0.004	0.017 ± 0.001	0.046 ± 0.003	0.050 ± 0.007
$\alpha$ (s mm $^{-1}$ )	0.092 ± 0.007	0.076 ± 0.014	0.113 ± 0.021	0.074 ± 0.002

**TABLE 4. Estimated parameters of Model III-B.**

	Case 1	Case 2	Case 3	Case 4
$\sigma_0$ (N mm $^{-1}$ )	1.203 ± 0.157	0.559 ± 0.266	1.818 ± 0.143	0.763 ± 0.092
$\sigma_1$ (N s mm $^{-1}$ )	0.374 ± 0.017	0.255 ± 0.063	0.581 ± 0.046	0.287 ± 0.030
$\sigma_2$ (N s)	0.014 ± 0.004	0.012 ± 0.001	0.010 ± 0.002	0.028 ± 0.001
$\mu_s$ (N)	0.788 ± 0.149	0.450 ± 0.028	0.667 ± 0.014	0.744 ± 0.026
$\mu_c$ (N)	0.033 ± 0.003	0.018 ± 0.008	0.041 ± 0.002	0.048 ± 0.006
$\alpha$ (s mm $^{-1}$ )	0.088 ± 0.010	0.074 ± 0.006	0.135 ± 0.006	0.072 ± 0.005

**TABLE 5. Averaged RMSE of friction force estimation in artificial phantom study (mN).**

	Case study	Model I	Model II	Model III-B	Karnopp model
Total	Case 1	29.7	19.6	17.9	28.2
	Case 2	23.1	14.5	13.3	22.9
	Case 3	27.0	19.2	15.8	21.8
	Case 4	49.3	30.9	28.1	39.8
Low range	Case 1	37.7	15.9	18.1	38.9
	Case 2	30.1	11.8	11.6	31.4
	Case 3	33.0	18.5	17.6	29.4
	Case 4	51.8	21.2	26.6	52.3
High range	Case 1	25.1	21.1	17.8	21.2
	Case 2	19.0	16.0	13.5	17.5
	Case 3	23.5	20.0	14.3	17.0
	Case 4	48.0	34.5	28.7	32.3

and inertial effect meaning that we can estimate the cutting force if the frictional effects are accurately modeled. Thus, as a potential advantage of our scheme, the cutting force can be simply obtained by deducting the estimated friction and inertial term from the totally measured interaction force.

In the experiments carried out in section “Friction Identification Using an Artificial Phantom,” the needle tip protruded from the tissue container hence no major cutting was present. This is not the case here since the

tip cuts the tissue during the first cycle(s) of penetration. Referring to Fig. 7a, within the very first seconds of motion, cutting occurred which was indicated by the major cutting regions. Substantial cutting also existed in the second profile as highlighted before 10 s during needle penetration into fresh tissue. According to Fig. 7a, minor cutting as a result of unpredicted needle–tissue interaction was found to be present in the third and fourth negative lobes of insertion. Here, due to the tip shape, needle deflection was small, and could

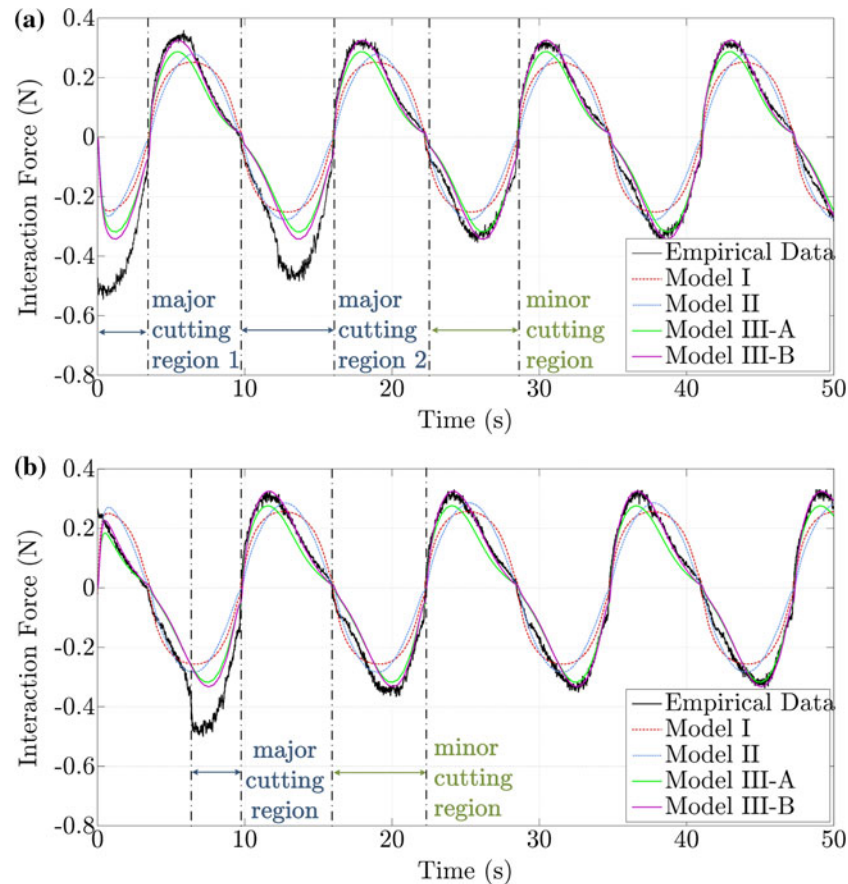


**FIGURE 7.** Predicted and measured interaction force: needle B/tissue A,  $f_{in} = 0.08$  Hz, and  $d_{in} = 25$  mm (case 2): (a) solid profile (b) dashed profile.

**TABLE 6.** Averaged RMSE of friction force prediction in artificial phantom study (mN).

	Solid profile		Dashed profile	
	Case 1	Case 2	Case 1	Case 2
Model I	79.0	68.9	74.7	62.8
Model II	73.1	67.0	75.6	68.7
Model III-A	39.2	31.5	55.3	35.7
Model III-B	41.9	22.8	51.6	29.0

be ignored from calculations as we have done. However, the slight bending that was not easy to predict caused the needle to cut fresh tissue. Consequently, an extra cutting force with a random pattern was introduced during the periodic insertion phase denoted by minor cutting in Fig. 7. Herein, the force prediction error can be mainly attributed to the cutting effect.

From the graphs, it is evident that the distributed solution, i.e., Model III, exhibits reasonably accurate results. Both versions of this model maintained close levels of accuracy albeit version B performed slightly better. Another observation was the inability of the

lumped version (Model II) to provide a good friction tracking while its accuracy was unexpectedly as low as the static structure (Model I). Model II presented a good estimation of the friction loop in section “Friction Identification Using an Artificial Phantom.” However, lack of an explicit term of the time-varying inserted length in (13) turned out to degrade accuracy here. It is worth noting that some of the conditions applied for the ease of implementation, e.g., the simplified boundary conditions introduced in section “Proposed Lure-Based Structures,” make a perfect match impossible. This suggests that  $f_n(\zeta)$  or  $\psi(\zeta)$  may

have complex functional shapes in reality that need further investigation.

### Friction Identification in Organic Tissues

Living tissues exhibit complex behaviors. In section “[Friction Identification Using an Artificial Phantom](#),” due to the relative rigidity of the employed sample, tissue motion was negligible. However, organic tissues are expected to deform substantially. The mechanism introduced in Asadian *et al.*<sup>7</sup> by the authors was employed in this paper to compensate for the relative velocity between a moving needle and deformable tissue. This technique allows us to formulate translational friction with respect to the insertion rate without imposing further complexities in tracking the entire soft tissue motion. For more details, refer to Asadian *et al.*<sup>7</sup>

We repeated a similar set of experiments using gelatin samples of differing concentrations (4–8%). Gelatin is an organic artificial substance whose main ingredients are bone and pig skin. Compared to the Gellan gum, the gelatin-made phantom deformed considerably, and exhibited a smoother force pattern with a negligible Stribeck effect. By tuning the slow observer introduced in Asadian *et al.*,<sup>7</sup> the distributed friction in 5% gelatin ( $E = 5.57 \text{ kPa}$ ) was successfully predicted as illustrated in Figs. 8a and 8b. At the next stage, beef liver was examined. The liver was the least stiff tissue ( $E = 1.89 \text{ kPa}$ ) in our experiments, and deformed the most. In this case, it was observed that the dynamics of tissue relaxation and friction mixed together lead to a wide force–velocity mapping; thus, a very slow velocity observer was employed to track the tissue motion. Figs. 8c and 8d show the measured and the estimated loops in terms of the estimated needle velocity and the estimated needle–tissue relative velocity in liver tissue. Accordingly, in beef liver, the friction force could be represented approximately by a single viscous term while the hysteresis was found to be negligible with respect to the estimated needle–tissue relative velocity. The Stribeck effect was also absent which may stem from the high internal lubrication of the organ due to blood. Table 7 also summarizes the numerical results using organic phantoms.

Consequently, our approach yielded good results at a wide range of insertion frequencies and amplitudes although tissue inhomogeneity in the liver case led to relatively large standard deviation values of the estimated parameters. Due to space limitations, only one set of results is reported here.

We also performed extensive *ex vivo* experiments on other animal tissues. In each case, tissue membrane

and fat layers were initially removed. Fresh muscle including chicken breast, beef, and pig ham produced identical force–velocity loops whose dynamics differed from the cycles generated by the LuGre model(s). For example, in our extended experiments on these three types of muscle tissue, it was observed that the equivalent Stribeck effect appeared very slowly, and viscous damping turned out to be negative (or zero) that were not justifiable by conventional friction theories. This suggests that mechanics of translational friction in muscle-like materials deserves more theoretical work. It is likely that we need to look at the problem at a molecular level in order to identify and then classify the structural components of a specific type of organic tissue. The authors believe that this is a challenging area in materials science and demands further study. Guidelines provided in Lister *et al.*<sup>17</sup> and Mahyah and Dupont<sup>18</sup> can be helpful since tissue inhomogeneity and nonlinearity contribute to greater complexity in analyzing of living tissue. The case studies presented in this work showed how the proposed approach can accommodate and deal with a wide range of friction dynamics in needle–tissue interaction without excessive complexity.

## CONCLUDING REMARKS AND FUTURE WORK

This paper presented a sophisticated approach to study and model features of translational friction during needle–tissue interaction. The interaction between the needle and soft tissue comprises frictional effects, and exhibits hysteresis loops. We showed that static friction mappings were inadequate for describing the existing transient nature. On the other hand, the proposed family of single-state distributed models as alternatives were capable of rendering the friction dynamics along the needle shaft. In practice, they performed well in a number of organic and artificial phantoms, e.g., Gellan gum, gelatin, and beef liver, while preserving favorable static and dynamic properties. The proposed models were developed by extending the well-known LuGre point friction model to the case of a moving contact patch along the insertion depth. Overall, the close match between the measured and the estimated friction forces presented in this paper proved the capability of our approach to mimic friction complexities. Furthermore, the proposed structure facilitated approximating the cutting force in an intra-operative manner.

In our study, due to the shape of the needle tip, bending was negligible, but future work will explore the effect of the distributed friction on bending

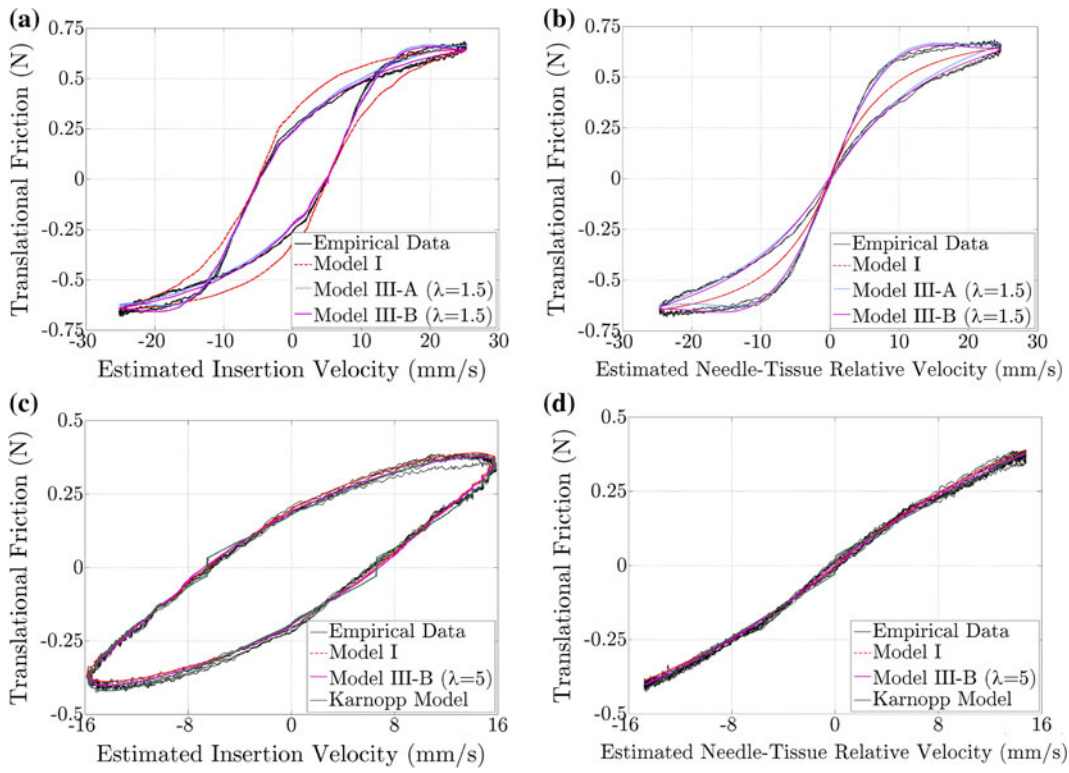


**FIGURE 8.** Experimental and identified cycles: (a) reconstructed friction vs. needle insertion velocity using needle A/gelatin (5% concentration),  $f_{in} = 0.1$  Hz, and  $d_{in} = 40$  mm, (b) friction vs. needle–tissue relative velocity using needle A/gelatin (5% concentration),  $f_{in} = 0.1$  Hz, and  $d_{in} = 40$  mm, (c) reconstructed friction vs. needle insertion velocity using needle A/beef liver,  $f_{in} = 0.1$  Hz, and  $d_{in} = 25$  mm, (d) friction vs. needle–tissue relative velocity using needle A/beef liver,  $f_{in} = 0.1$  Hz, and  $d_{in} = 25$  mm.

**TABLE 7.** Averaged RMSE of friction force estimation using organic phantoms (mN).

Case study	Model I	Model III-A	Model III-B	Karnopp model
Needle A/gelatin	64.4	24.1 ( $\lambda = 1.5$ )	18.1 ( $\lambda = 1.5$ )	—
Needle A/beef liver	16.1	—	12.3 ( $\lambda = 5$ )	14.5

dynamics of a bevel-tip needle. Friction modeling is believed to be a crucial step toward automating needle guidance in live tissues, and the method developed in this paper enable us to refine the beam-based deflection models in which full frictional effects are ignored.<sup>2</sup> Although not very accurate, these static models are widely exploited for the purpose of steering<sup>3,13,28</sup> due to their simplicity and computational efficiency. In order to steer a flexible needle, clinicians will likely have to slow down the insertion and rotate the needle with variable insertion rates before further actions. Thus, path deviation as a result of unmodeled friction can cause planning inaccuracy. Related research by the authors is reported in Asadian *et al.*<sup>4</sup> in which only the viscous term was accounted for in needle deflection.

In the experiments conducted, the frictional effects during needle insertion were found to be considerable. Furthermore, significant differences were observed

between the phantoms either artificial or organic. Considering these empirical observations, exploring a new artificial phantom as a mixture of chemicals that produces a more realistic force pattern would be of value. It will certainly ease and accelerate the process of developing new modeling and guidance mechanisms in interventional procedures. As is obvious, managing experiments on animal organs under controlled or repeatable conditions is challenging and requires addressing practical issues including (1) storage and contamination; (2) precise cutting and fitting the sample into its container, and (3) tissue immobilization. That is why artificial phantoms are usually preferred as the very first steps in validating a new approach. An ideal artificial phantom is expected to preserve the typical range of elasticity, viscosity and tissue deformation of living tissues as well as replicating its force–velocity dynamics. Another aspect of our

future work involves validation of the results using other animal organs such as lung and kidney. In the case of inhomogeneous phantoms, the dynamics of tissue puncture may have considerable effect on the entire needle–tissue interaction, especially for multi-layer tissue. This also requires further in-depth investigation.

## ACKNOWLEDGMENTS

A part of the work described in this paper was presented at the IEEE International Conference on Robotics and Automation (ICRA), Shanghai, China, 2011. Financial support for A. Asadian was also provided by an NSERC Collaborative Research and Training Experience (CREATE) Program Grant #371322-2009 in Computer-Assisted Medical Interventions (CAMI).

## REFERENCES

- <sup>1</sup>Abolhassani, N., R. Patel, and M. Moallem. Needle insertion into soft tissue: a survey. *Med. Eng. Phys.* 29:413–431, 2007.
- <sup>2</sup>Abolhassani, N., R. V. Patel, and F. Ayazi. Minimization of needle deflection in robot-assisted percutaneous therapy. *Int. J. Med. Robot. Comput. Assist. Surg.* 3:140–148, 2007.
- <sup>3</sup>Alterovitz, R., M. Branicky, and K. Goldberg. Motion planning under uncertainty for image-guided medical needle steering. *Int. J. Robot. Res.* 27(11–12):1361–1374, 2008.
- <sup>4</sup>Asadian, A., M. R. Kermani, and R. V. Patel. An analytical model for deflection of flexible needles during needle insertion. In: IEEE/RSJ International Conference on Intelligent Robots and Systems. 2011, pp. 2551–2556.
- <sup>5</sup>Asadian, A., M. R. Kermani, and R. V. Patel. A novel force modeling scheme for needle insertion using multiple Kalman filters. *IEEE Trans. Instrum. Meas.* 61(2):429–438, 2012.
- <sup>6</sup>Asadian, A., R. V. Patel, and M. R. Kermani. A distributed model for needle–tissue friction in percutaneous interventions. In: IEEE International Conference on Robotics and Automation. 2011, pp. 1896–1901.
- <sup>7</sup>Asadian, A., R. V. Patel, and M. R. Kermani. Compensation for relative velocity between needle and soft tissue for friction modeling in needle insertion. In: IEEE EMBS Annual International Conference. 2012, pp. 960–963.
- <sup>8</sup>Barbe, L., B. Bayle, and M. de Mathelin. In vivo model estimation and haptic characterization of needle insertions. *Int. J. Robot. Res.* 26(11–12):1283–1301, 2007.
- <sup>9</sup>Bassan, H. S., R. V. Patel, and M. Moallem. A novel manipulator for percutaneous needle insertion: design and experimentation. *IEEE/ASME Trans. Mechatron.* 14(6):746–761, 2009.
- <sup>10</sup>Canudas De Wit, C., H. Olsson, K. J. Astrom, and P. Lischinsky. A new model for control of systems with friction. *IEEE Trans. Automat. Contr.* 40:419–425, 1995.
- <sup>11</sup>Canudas De Wit, C., P. Tsotras, E. Velenis, M. Basset, and G. Gissinger. Dynamic friction models for road/tire longitudinal interaction. *Veh. Syst. Dyn.* 39(3):189–226, 2003.
- <sup>12</sup>DiMaio, S. P., and S. E. Salcudean. Needle insertion modelling and simulation. *IEEE Trans. Robot. Autom.* 19(5):864–875, 2003.
- <sup>13</sup>Duindam, V., J. Xu, R. Alterovitz, S. Sastry, and K. Goldberg. Three-dimensional motion planning algorithms for steerable needles using inverse kinematics. *Int. J. Robot. Res.* 29:789–800, 2010.
- <sup>14</sup>Hing, J. T., A. D. Brooks, and J. P. Desai. Reality-based estimation of needle and soft-tissue interaction for accurate haptic feedback in prostate brachytherapy simulation. *Springer Tracts Adv Robot.* 28:34–48, 2007.
- <sup>15</sup>Kataoka, H., T. Washio, K. Chinzei, K. Mizuhara, C. Simone, and A. M. Okamura. Measurement of the tip and friction force acting on a needle during penetration. In: International Conference on Medical Image Computing and Computer Assisted Intervention. 2002, pp. 216–223.
- <sup>16</sup>Kermani, M. R., R. V. Patel, and M. Moallem. Friction identification and compensation in robotic manipulators. *IEEE Trans. Instrum. Meas.* 56(6):2346–2353, 2006.
- <sup>17</sup>Lister, K., Z. Gao, and J. P. Desai. Development of in vivo constitutive models for liver: application to surgical simulation. *Ann. Biomed. Eng.* 39(3):1060–1073, 2011.
- <sup>18</sup>Mahvah, M., and P. E. Dupont. Mechanics of dynamic needle insertion into a biological material. *IEEE Trans. Biomed. Eng.* 57(4):934–943, 2010.
- <sup>19</sup>Misra, S., K. T. Ramesh, and A. M. Okamura. Modeling of tool–tissue interactions for computer-based surgical simulation: a literature review. *Presence Teleop. Virt.* 17(5):463–491, 2008.
- <sup>20</sup>Okamura, A. M., C. Simone, and M. D. O’Leary. Force modeling for needle insertion into soft tissue. *IEEE Trans. Biomed. Eng.* 51(10):1707–1716, 2004.
- <sup>21</sup>Olsson, H., K. J. Astrom, C. Canudas De Wit, M. Gafvert, and P. Lichinsky. Friction models and friction compensation. *Eur. J. Control.* 4(3):176–195, 1998.
- <sup>22</sup>Podder, T. K., J. Sherman, E. M. Messing, D. J. Rubens, D. Fuller, J. G. Strang, R. A. Brasacchio, and Y. Yu. Needle insertion force estimation model using procedure-specific and patient-specific criteria. In: IEEE EMBS Annual International Conference. 2006, pp. 555–558.
- <sup>23</sup>Reed, K. B., A. M. Okamura, and N. J. Cowan. Modeling and control of needles with torsional friction. *IEEE Trans. Biomed. Eng.* 56(12):2905–2916, 2009.
- <sup>24</sup>Roesthuis, R. J., Y. R. J. van Veen, A. Jahya, and S. Misra. Mechanics of needle–tissue interaction. IEEE/RSJ International Conference on Intelligent Robots and Systems. 2011, pp. 2557–2563.
- <sup>25</sup>Ross, K. A., and M. G. Scanlon. Analysis of the elastic modulus of agar gel by indentation. *J. Texture Stud.* 30(1):17–27, 1999.
- <sup>26</sup>Van Gerwen, D. J., J. Dankelman, and J. J. van den Dobbelaer. Needle–tissue interaction forces: a survey of experimental data. *Med. Eng. Phys.* 34:665–680, 2012.
- <sup>27</sup>Webster III R. J., J. S. Kim, N. J. Cowan, G. S. Chirikjian, and A. M. Okamura. Nonholonomic modeling of needle steering. *Int. J. Robot. Res.* 25:509–525, 2006.
- <sup>28</sup>Wood, N. A., K. Shahrouz, M. C. Ost, and C. N. Riviere. Needle steering system using duty-cycled rotation for percutaneous kidney access. *IEEE EMBS Annual International Conference* 2010, pp. 5432–5435.